RAINFALL DETECTION USING THE INFRARED BANDS OF HIMAWARI-8 ADVANCED HIMAWARI IMAGER IN THE PHILIPPINES

Redmund G. Nacario[1], Gay Jane Perez, Ph. D.[2], and Gerry Bagtasa, Ph. D.[3]

[1, 2, 3]Institute of Environmental Science and Meteorology,
University of the Philippines Diliman,
P. Velasquez Street, U.P Campus Diliman, Quezon City, 1101, Metro Manila, Philippines
Email: [1] redmund.nacario@gmail.com, [2] ggperez1@up.edu.ph,
& [3] gerrybagtasa@gmail.com

KEY WORDS: Brightness temperature differences, Geostationary satellite, Ground-based weather Radar, Look-up table

ABSTRACT: This study examined the utilization of infrared bands (IR) from Himawari-8 Advanced Himawari Imager (AHI) for rainfall area detection in the Philippines. The parameters used include the IR brightness temperature (BT) at 10.4 microns ($T_{10.4}$) and several IR BT differences (BTD), which were inferred as proxies for cloud properties such as cloud top height, cloud optical thickness, cloud water path, and cloud phase. These cloud properties were used to create a Probability of Rain (POR) look-up table (LUT) together with processed horizontal reflectivity radar data gathered on rainy periods of July to September 2015. Combinations of BTD's for POR LUT construction includes the simple BTD's, BTD's based on cloud property, and selected BTD's. Rain detection assessment using different skill scores showed an increased performance of POR LUT with selected BTD combinations compared to with simple BTD's in training and testing stage. This is attributed to the increase in the sensitivity of detecting rain due to additional BTD. In visual comparison with Global Satellite Mapping of Precipitation (GSMaP) hourly rainfall maps, the POR LUT dominated by cloud-top height produced rain maps with high similarity. Prominent thin cirrus clouds and cold cloud dense overcast of the typhoons in testing stage were successfully classified as no-rain and rain, respectively. However, high false alarm rates were obtained when compared to radar data which means an over estimation of the method on rain detection. This is due to the weakness of weather radar on detecting rainfall in partially or fully blocked areas by mountains present in the domain, and the high variability of rain occurrences. The POR LUT using the selected BTD combinations dominated by cloud-top height is a viable method for satellite-based rainfall rate estimation due to its superiority to simple BTD combinations.

1. INTRODUCTION

Precipitation is defined as the water released from clouds in the form of rain, freezing rain, sleet, snow, or hail. It is one of the major processes in Earth's water and energy cycle in which it delivers atmospheric water to the Earth surface. In the tropical region, most precipitation falls as rain. Philippines, located inside the tropical region, experiences rainfall events caused by low pressure systems like tropical cyclones, monsoon rains, localized thunderstorms, mesoscale convective storms, and Inter-tropical convergence zone. These weather processes contributed to the mean annual rainfall amount varying from 965 to 4,054 millimeters (PAGASA, 2015).

The most destructive effects of extreme rain events are torrential rainfall amounts, severe floods and landslides within a short period of consecutive days. An example is during Typhoon *Ketsana* which instigated flash floods over Metropolitan Manila and neighbouring provinces on September 24 - 27, 2009. Another is the Southwest monsoon or *Habagat* rain episodes on August 2012 and 2013 which also brought heavy rainfall causing floods over the same areas. The recorded rainfall amounts from *Habagat* rain episodes rapidly exceeded the normal rainfall value in August.

The impacts of extreme rainfall events can be minimized with the use of observations from remote sensing satellites. Satellites provide timely monitoring and continuous spatial coverage of cloud patterns, thus, can be used for rainfall detection. Known methods in remote sensing utilizing different bands in electromagnetic (EM) spectrum for precipitation detection and measurement is composed of visible (VIS), near-infrared (NIR), IR, passive microwave (PM), and combination of these bands. Among these, PM rain data are found to be directly related to rain rate (Anagnostou, 2004). Nevertheless, PM sensors, which are commonly aboard polar-orbiting satellites, is limited with coarse spatial resolutions of data, and narrow coverage. These attributes are opposite to VIS, NIR and IR techniques. VIS, NIR and IR sensors, aboard geostationary satellites, can detect precipitation rates with time intervals of minutes to hours, with high spatial resolution from four kilometers to one kilometer, and with wide spatial domain. Though VIS, NIR and IR measurements are poorly related to precipitation (Kidd & Levizzani, 2011), it can be related to cloud-top texture, optical-cloud thickness, and effective particle radius (Kuhnlein *et al*., 2010). These are cloud

properties which can be associated with rainfall rate. The detection of IR EM waves on both night-time and daytime provides a consistent data source for continuous real-time rain monitoring.

1.1 Application of Himawari - 8 AHI

The new geostationary satellite of Japan known as Himawari-8, with its sensor Advanced Himawari Imager (AHI), offers better spatial and temporal resolution and more spectral bands compared to its predecessor, the Multi-functional Transport Satellite (MTSAT). AHI can observe Earth's atmosphere using 16 bands, specifically: 3 VIS bands, 3 NIR bands, and 10 IR bands (Bessho *et al*., 2016). From MTSAT previous four kilometers grid resolution, a finer resolution of 0.5 to one kilometers and two kilometers for VIS/NIR and IR bands, respectively can now be measured by AHI. Furthermore, a temporal resolution of ten minutes provides real time monitoring of rainfall and cloud activities. The AHI spectral bands especially the IR channel are currently untapped for rainfall estimation researches. This study seeks to use AHI's IR channel BTs and BTDs for rain detection within the Philippines.

Based on several related studies summarized in Table 1, IR BTD's can be a proxy of cloud properties. These cloud properties include cloud-top height, cloud optical thickness, cloud phase, and cloud water path. The wide range of IR bands present in AHI led to the formulation of this study which examines the capability of Himawari-8 AHI IR BTD for rainfall detection. Specifically, this study aims to develop POR LUT using IR BTD from AHI with reflectivity data of Tagaytay radar in the Philippines. It also aims to determine the best combination of IR BTD's as component of POR LUT by assessing its performance in the training and testing stage.

Table 1. Related studies of the IR BTD inferred as a proxy of cloud property.

Cloud property	**BTD**	**AHI IR BTD**	**Studies**
Cloud-top height	$T_{6.2-10.8}$	$T_{6.2-10.4}$	Kurino, 1997; Lutz *et al*., 2003
	$T_{6.2-7.3}$	$T_{6.2-7.3}$	Santurette & Georgiev, 2007
	$T_{13.4-10.8}$	$T_{13.3-10.4}$	Mecikalski *et al*., 2007; Mecikalski & Bedka, 2006
	$T_{9.7-13.4}$	$T_{9.6-13.3}$	Kwon *et al*., 2010
Cloud optical thickness	$T_{10.8-12.1}$	$T_{10.4-12.3}$	Inoue, 1985, 1987, & 2001; Thies *et al*., 2008a & 2008b
	$T_{8.7-12.1}$	$T_{8.6-12.3}$	Krebs *et al*., 2007, Strabala *et al*., 1994
Cloud phase	$T_{8.7-10.8}$	$T_{8.6-10.4}$	Thies *et al*., 2008a & 2008b; Baum & Platnick, 2006
Cloud water path	$T_{3.9-10.8}$	$T_{3.9-10.4}$	Lensky & Rosenfeld, 2003a; Thies *et al*., 2008a
	$T_{3.9-7.3}$	$T_{3.9-7.3}$	Thies *et al*., 2008a

2. METHODOLOGY

Derived IR BTD from AHI and reflectivity data from radar were pre-processed and were used as an input to the development of POR LUT. Different BTD combinations in this process were utilized, thus, creating different LUT's. These POR LUT's were used to produce POR maps, and rainfall maps in training and testing stage. In the training stage, the optimum POR threshold were determined and assessed to classify rain from no-rain. Furthermore, these thresholds found were assessed in the testing stage. A qualitative comparison of the resulting rainfall maps with another satellite rainfall data known as GSMaP hourly rainfall data was done to visually assess the output maps within the domain of the Philippines.

2.1 Data and Area of Study

The data used in this study includes the IR BTD from Himawari-8 AHI (Table 1), the constant altitude plan-position indicator (CAPPI) product at 3km altitude of horizontal reflectivity from Tagaytay C-band radar, and the GSMaP rainfall rate product. These collected datasets extend from months of July to December 2015. The region of interest is within Tagaytay radar coverage of the Philippines, encompassing a circular area with 120 km radius from coordinates 14.123 °N 120. 974 °E (Figure 1).

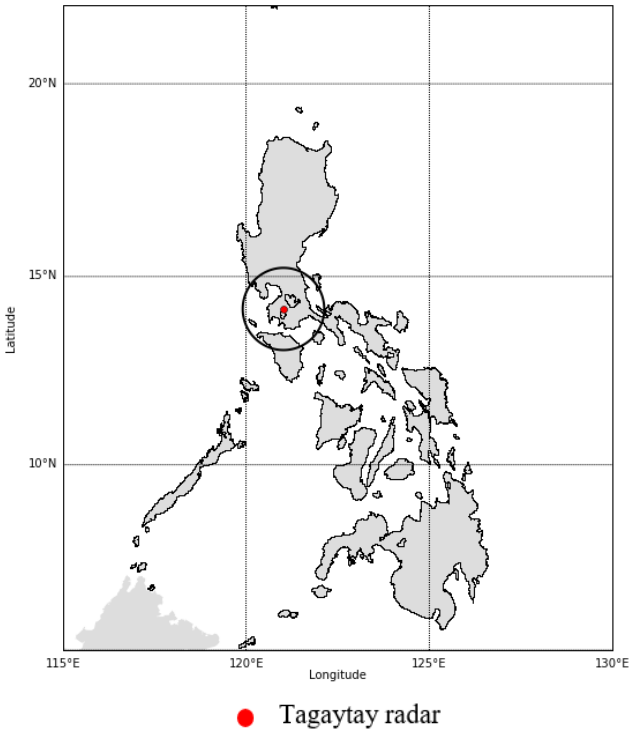

Figure 1. The region of interest.

Training and Testing datasets: The datasets in the study were grouped separately based on its purpose such as training and testing stages. The training datasets, which were used in creating POR LUT, covers the rainy periods on July to September 2015. In this period, typhoons, thunderstorms and Southwest monsoon rains occur in the Philippines. The testing dataset, on the other hand, are gathered from selected dates of rain events caused by typhoon occurrences within the temporal coverage of the study. Specifically, the testing dataset consists of occurrences of tropical cyclones on year 2015 named as *Mujigae* from October 1 – 4, *Koppu* from October 18 - 19, and *Melor* from December 14 – 17.

2.2 Probability of Rain (POR) LUT

POR is defined as the percentage value of rain event frequency over the total number of events. The equation is presented as:

$$POR(x_1,\ldots, x_n)= \frac{N_{rain}(x_1,\ldots, x_n)}{N_{rain}(x_1,\ldots, x_n)+ N_{no\text{-}rain}(x_1,\ldots, x_n)} \quad (1)$$

Where $(x_1,\ldots, x_n)$ are the combination of BTD, and $N_{rain}(x_1,\ldots, x_n)$ and $N_{no\text{-}rain}(x_1,\ldots, x_n)$ are the number of pixels with rain and with no –rain denoted by $(x_1,\ldots, x_n)$ respectively.

Computation of POR was done through temporal matching of BTD maps with the reflectivity maps. The radar reflectivity data identifies and assigns rain pixels to the spatially equivalent BTD pixels. The rain pixels with BTD values, will be grouped depending on the pre-determined range bin of each BTD, thus produces a distribution of frequency of rain events. The process is also the same with non-raining pixels. These matrices are combined together using Equation 1 to form a POR distribution as a function of BTD combinations. By setting the threshold in POR distribution, the LUT can be used on satellite input images to derive a binary map classifying rain from no-rain areas.

2.3 Experimental Design

BTD combinations, used for POR LUT creation, are grouped into three: simple BTD combinations, combinations based on cloud property, and selected BTD combinations (Table2). The **s**imple BTD combinations are consists of individual BTD along with BT at $T_{10.4}$. The selected BTD combinations were based on the individual performance of simple BTD combinations found in this study. Each BTD combinations produced an LUT which in turn can be utilized to create maps with rain and no-rain areas.

Table 2. Selected BTD combinations used in creation of POR LUT

Group	Label	BTD combinations
Simple BTD combinations	CTH1	$T_{6.2 - 10.4}$ & $T_{10.4}$
	CTH2	$T_{6.2 - 7.3}$ & $T_{10.4}$
	CTH3	$T_{13.3- 10.4}$ & $T_{10.4}$
	CTH4	$T_{9.6-13.3}$ & $T_{10.4}$
	COT1	$T_{10.4-12.3}$ & $T_{10.4}$
	COT2	$T_{8.6-12.3}$ & $T_{10.4}$
	CP	$T_{8.6-10.4}$ & $T_{10.4}$
Combinations based on cloud property	CWP	$T_{3.9-10.4}$ & $T_{10.4}$
	CWP	$T_{3.9-7.3}$ & $T_{10.4}$
	CTH	All CTH & $T_{10.4}$
	COT	All COT & $T_{10.4}$
	CWP	All CWP & $T_{10.4}$
Selected BTD combinations	BTD1	All CTH & $T_{10.4}$
	BTD2	CTH3, CWP2, COT1, & $T_{10.4}$
	BTD3	CTH3, CWP2, CP, & $T_{10.4}$
	BTD4	COT1, CWP2, CP, & $T_{10.4}$
	BTD_all	All BTD & $T_{10.4}$

2.4 Skill Scores

Different statistical skill scores were used in the study to determine the overall performance of the methods used for classifying rain from no-rain areas in both training and testing stage (Feidas, & Giannakos, 2010). These scores were based on the contingency table indicated on Table 3. Hits and Zeros are both correctly identified rain and no-rain events respectively while False Alarms and Misses are not. The different skill scores were listed in Table 4.

Table 3. Contingency table.

Forecasted or Estimated	Observed	
	Rain	No-rain
Rain	Hits (A)	False Alarms (B)
No-rain	Misses (C)	Zeros (D)

Table 4. Different Skill Scores used in the study.

Skill Scores	Equations	
Probability of Detection	$POD = \frac{A}{A + B}$	(2)
False Alarm Ratio	$FAR = \frac{B}{A + B}$	(3)
Probability of False Detection	$POFD = \frac{B}{B + D}$	(4)
Critical Success Index	$CSI = \frac{A}{A + B + C}$	(5)
Equitable Threat Score	$ETS = \frac{(A \times D) - (B \times C)}{(B + C)N + ((A \times D) - (B \times C))}$	(6)
Hanssen and Kuipers score	$HK = \frac{(A \times D) - (B \times C)}{(B + D)(A + C)}$	(7)
Relative Operating Characteristic (ROC) Distance	$distance(T_1,\ldots, T_n) = \sqrt{\left(POFD - POFD_{(T_1,\ldots, T_n)}\right)^2 + \left(POD - POD_{(T_1, \ldots, T_n)}\right)^2}$	(8)

Normalized Skill Score (NSS): NSS determines the POR threshold based on the optimal combination of score values derived from CSI, ETS, HK, and ROC distance (Equation 9). This score was used only on the training stage. The NSS equation is shown below:

$$NSS(T_1, \ldots, T_n) = \frac{1}{4}\left(\frac{CSI(T_1, \ldots, T_n)}{CSI_{max}} + \frac{ETS(T_1, \ldots, T_n)}{ETS_{max}} + \frac{HK(T_1, \ldots, T_n)}{HK_{max}} + \frac{1\text{-distance}(T_1, \ldots, T_n)}{1\text{-distance}_{min}}\right) \quad (9)$$

In the above equation, the (T_1, …, T_n) are the varying POR threshold values, and the max and min denotes the maximum and minimum score of the indicated skill score, respectively. NSS values range from 0 to 1. NSS value of 1 denotes that all four skill scores agree in a single threshold value.

3. RESULTS

3.1 POR Threshold

In the training stage, POR threshold were determined in order to assess the performance of POR LUT in discriminating rain from no-rain areas. The 17 constructed POR LUT has its own optimum threshold based on skill scores. Figure 2 shows the variation of NSS, CSI, ETS, HK, & ROC distance in increasing POR threshold values in BTD_all. The threshold value were found to be in 0.32 with maximum NSS.

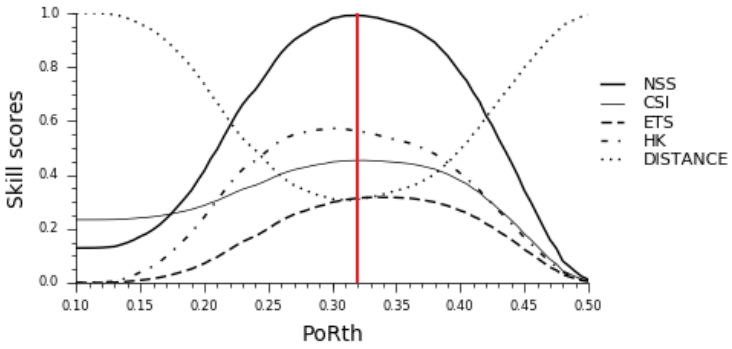

Figure 2. Variation of NSS, CSI, ETS, HK, & ROC distance with increasing POR threshold.

3.2 Training Stage

The resulting skill scores in training stage are shown in Figures 3, and 4. Among all BTD combinations, the CTH3 has the highest CSI, HK, ETS, and POD. The simple BTD combinations, except CTH3, does not perform well. On the other hand, the BTD combinations based on cloud property, except CTH, inherits the poor performance from its components thus resulting with low score on CSI, HK, ETS, and POD. The selected BTD combinations and CTH perform well in all scores with low POFD, which is a good characteristic compared to CTH3 with high false alarm rates. CTH scores is almost the same to BTD1 due to its similarity of BTD components.

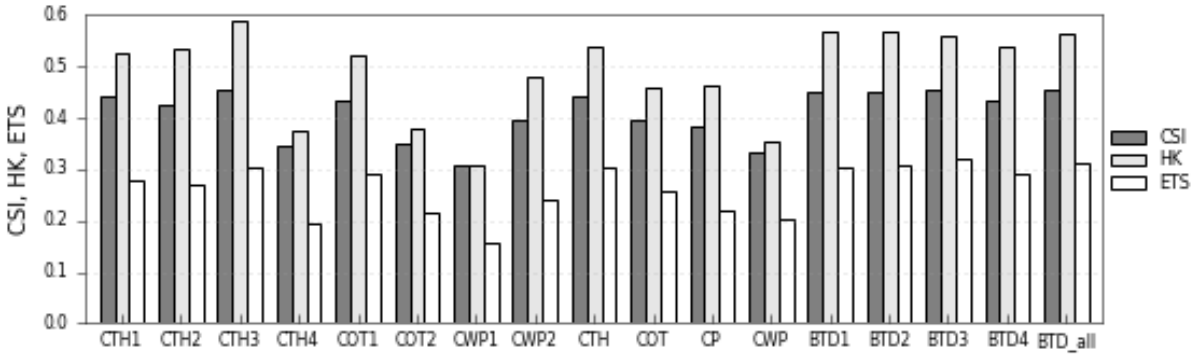

Figure 3. CSI, HK, and ETS scores of POR LUT outputs in training stage using different BTD combinations.

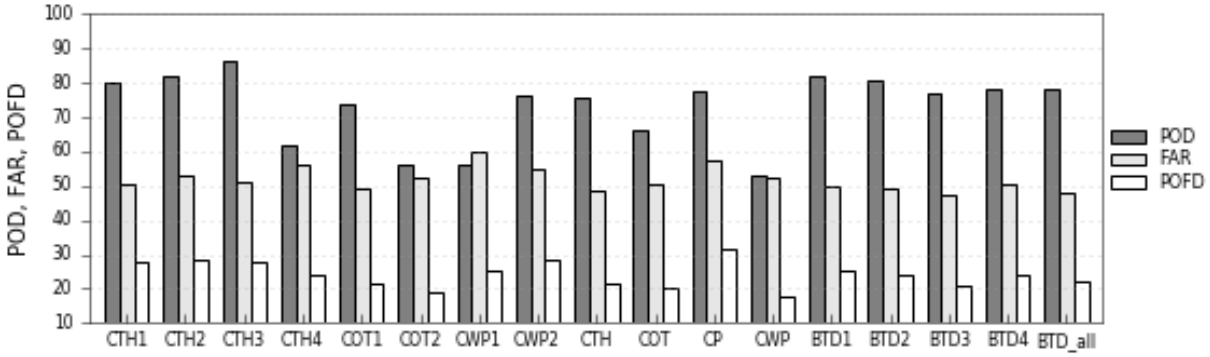

Figure 4. POD, FAR, and POFD scores of POR LUT outputs in training stage using different BTD combinations.

3.3 Testing Stage

The skill score results based on the POR BTD combinations for testing stage are shown in Figures 5 and 6. Almost similar general patterns on BTD combinations can be found from the results of training stage except on decreased CSI and ETS, and increased FAR and POFD. CTH3 and CTH4 does not perform consistently compared with the output in training stage. Notable increase in POD of CTH, BTD1, and BTD_all can be seen at the expense of increased POFD and FAR.

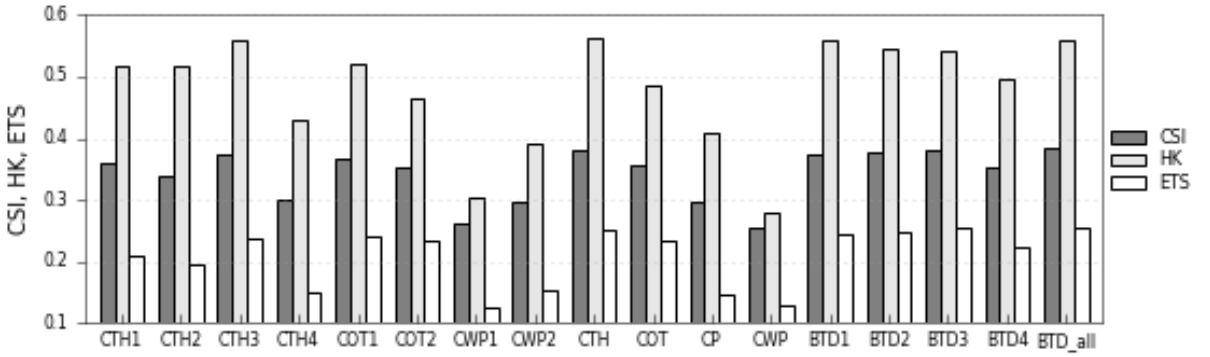

Figure 5. CSI, HK, and ETS scores of POR LUT outputs in testing stage using different BTD combinations.

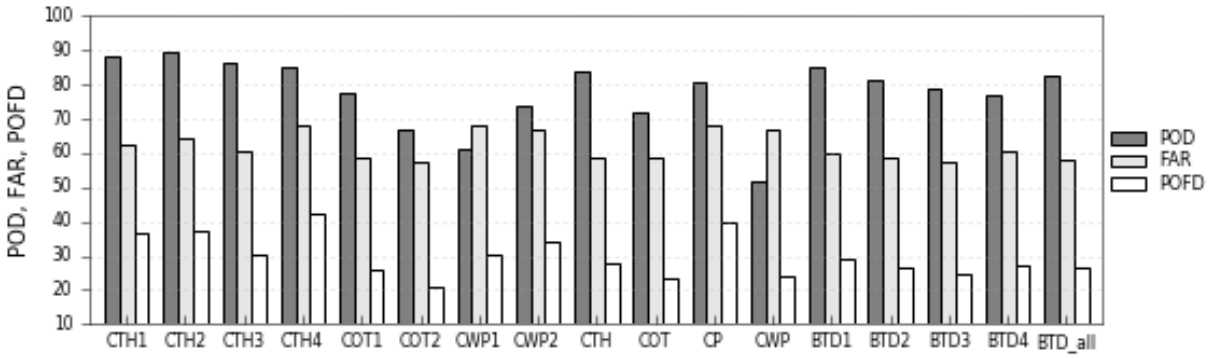

Figure 6. POD, FAR, and POFD scores of POR LUT outputs in testing stage using different BTD combinations.

3.4 Comparison with GSMaP MVK Rainfall Rate Product

Qualitative analysis was done through comparison of Himawari-8 $T_{10.4}$ image, and GSMaP MVK hourly rainfall product with the rain and no-rain map outputs of POR LUT. The selected BTD combinations were chosen due to its consistency and relatively good performance based on the skill scores found on testing and training stage. The qualitative comparison is shown in Figures 7, 8, and 9 depicting Typhoon *Mujigae*, *Koppu* and *Melor*, respectively.

Strong similarities were seen from the rainfall areas in GSMaP data and rain maps. However, BTD2, BTD3, and BTD4 showed a noisy behaviour outside and inside the regions of rainfall area depicted in GSMaP. Here, cirrus

clouds at Himawari $T_{10.4}$ images were misclassified as rains located outside the cloud dense of typhoons. Meanwhile, BTD_all, CTH, and BTD1 displays a satisfactory result among selected BTD combinations compared to GSMaP. In contrast with BTD2, BTD3, and BTD4, cirrus clouds are correctly classified as no rain by the BTD_all, CTH, and BTD1.

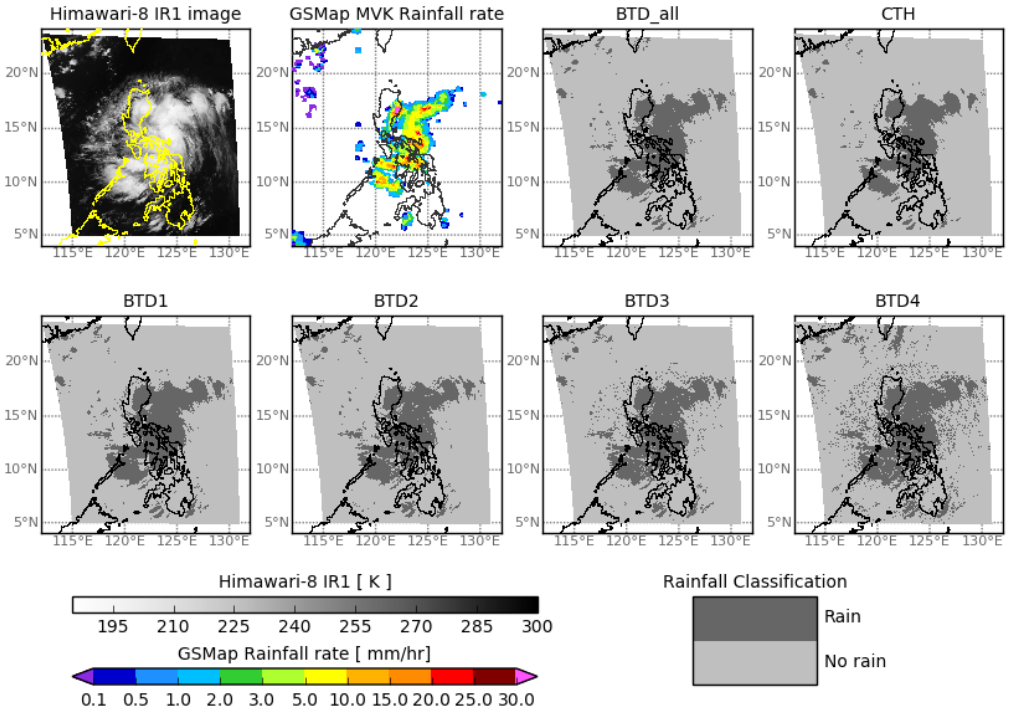

Figure 7. Comparison of GSMaP rainfall product to POR LUT output maps during Typhoon *Mujigae* on 2015-10-01 01:00 UTC.

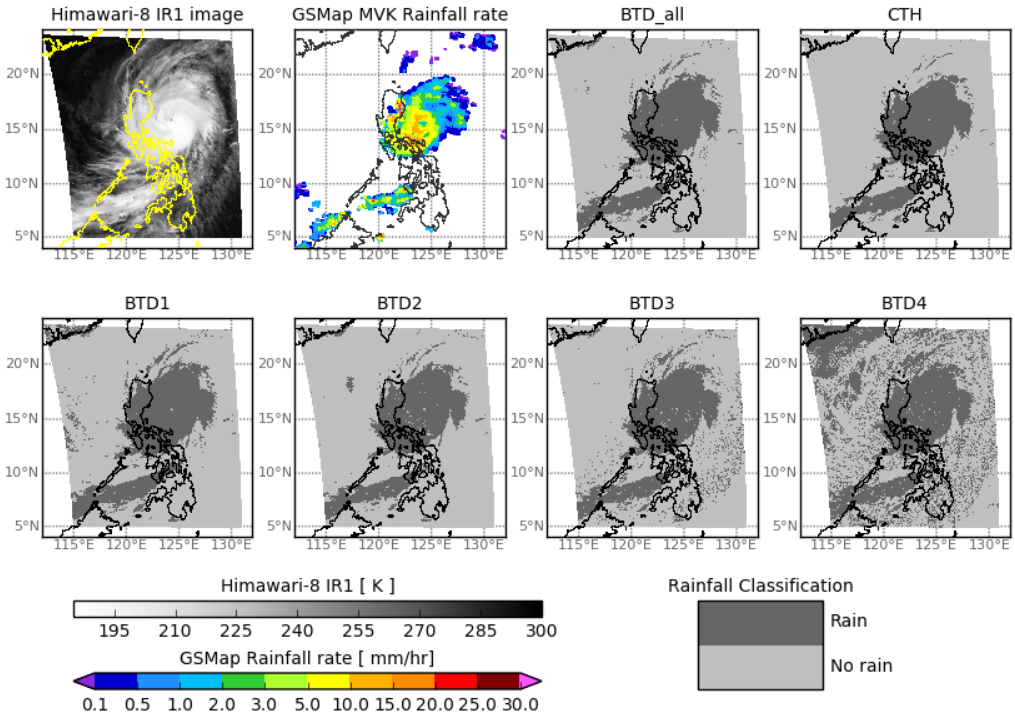

Figure 8. Comparison of GSMaP rainfall product to POR LUT output maps during Typhoon *Koppu* 2015-10-17 01:00 UTC.

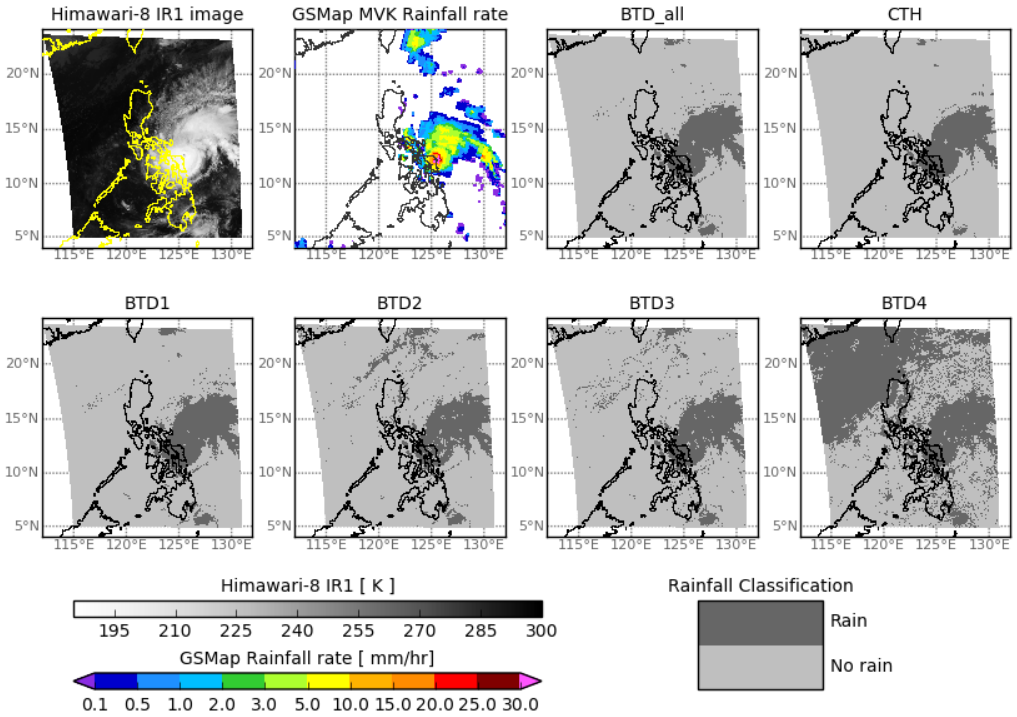

Figure 9. Comparison of GSMaP rainfall product to POR LUT output maps during Typhoon *Melor* 2015-12-14 01:00 UTC

4. DISCUSSIONS AND CONCLUSIONS

The application of Himawari-8 AHI IR bands for rainfall detection was examined. POR LUT method was used to derive rainfall maps from IR BTD. Several BTD combinations were used to construct POR LUT that includes simple combinations, combinations based on cloud property, and selected combinations. The rainfall outputs were compared with radar images using different skill scores and with GSMaP through qualitative analysis.

Results showed an increased performance on POR model with many BTD components in detection of rain and no-rain on training and testing stage compared to with few BTD. Increased POD, and decreased FAR and POFD were observed in selected BTD combinations. These behaviours can be attributed to the equation of POR which depends on the frequency of rain and no-rain events in the training dataset. However, over-estimation denoted by FAR score still persists. This can be caused by the limitation of radar data to detect rain in partially or fully blocked areas such as behind mountains existing on the radar domain which is in contrast, detected by POR method as rain. Also, number of false alarms of rain clouds on the method used is expected to happen due to high variability of rain occurrences. Though the POR LUT method on selected BTD combinations suffers consistent false alarms of rain, it is still superior to simple BTD combinations.

Rainfall map outputs from Selected BTD combinations were assessed through qualitative analysis with GSMaP data. CTH, BTD1 and BTD_all showed promising similarities with GSMaP data. Distinguishable thin cirrus clouds are tagged as no-rain in contrast with thicker and high clouds. The said BTD's are dominated by cloud-top height property which is directly related to the level of convection as seen in cold cloud dense overcast of Typhoons in Himawari-8 $T_{10.4}$ images (Figures 7 to 9). The effect of missing cloud-top height component of POR LUT was prominent in BTD4 rain images in which false classification occurs in regions far away from the typhoons. Cloud-top height is therefore the key component among BTD's used in POR model but other BTD's are important to minimize false alarms of rain events.

This study provides insights on application of AHI IR BTD in rainfall detection through LUT. The POR LUT can maximize the satellite images through emphasizing areas with important information like classification of rain and no-rain areas on Typhoon cases. The method can be used as initial step for satellite-based rainfall rate estimation. However, this study still needs of further investigation on different cases like rain caused by thunderstorms and other low pressure systems.

5. ACKNOWLEDGEMENT

This study acknowledges the Philippine government agencies under Department of Science and Technology (DOST) such as the Science Education Institute (SEI), the Advanced Science and Technology Institute (ASTI), the Philippine Atmospheric Geophysical and Astronomical Services Administration (PAGASA), and the Philippine Council for Industry and Energy Research and Development (PCIERD) through the project Remote Sensing Product Development (PHL MICROSAT Project 5). These offices provided the research grants, computing support, and data for the completion of study. Furthermore, a big appreciation to the Japan Aerospace Exploration Agency, and Japan Meteorological Agency who delivered the needed Himawari-8 data and support for data access.

6. REFERENCES

Anagnostou, E. N., 2004. Overview of overland satellite rainfall estimation for hydro-meteorological applications. Surveys in Geophysics, 25(5-6), 511–537.

Baum, B. A., Platnick, S., 2006. Introduction to MODIS cloud products. In: Qu JJ, GaoW, Kafatos M, Murphy RE, Salomonson VV (eds) Earth science satellite remote sensing: science and instruments. Springer, New York.

Bessho, K. *et al*., 2016. An introduction to Himawari-8/9 - Japan's new-generation geostationary meteorological satellites, Journal of the Meteorological Society of Japan, 94, doi:10.2151/jmsj.2016-009.

Feidas, H., & Giannakos, A., 2010. Identifying precipitating clouds in Greece using multispectral infrared Meteosat Second Generation satellite data. Theoretical and Applied Climatology, 104, 25–42.

Inoue, T., 1985. On the temperature and effective emissivity determination of semi-transparent cirrus clouds by bi-spectral measurements in the 10-mm window region. Journal of the Meteorological Society of Japan, 63, 88–99.

Inoue, T., 1987. A cloud type classification with NOAA-7 split- window measurements. J Geophys Res, 92, 3991–4000.

Inoue, T., Wu, X., & Bessho, K., 2001. Life cycle of convective activity in terms of cloud type observed by split window. 11th Conference on Satellite Meteorology and Oceanography, Madison, WI, USA.

Kidd, C., & Levizzani, V., 2011. Status of satellite precipitation retrievals. Hydrology and Earth System Sciences, 15(4), 1109–1116.

Krebs, W., Mannstein, H., Bugliaro, L., & Mayer, B., 2007. A new day and night time meteosat second generation cirrus detection algo- rithm mecida. Journal of Atmospheric Chemistry and Physics, 7, 10933–10969.

Kuhnlein, M., Thies, B., Nauß, T., & Bendix, J., 2010. Rainfall-rate assignment using MSG SEVIRI data-A promising approach to spaceborne rainfall-rate retrieval for midlatitudes. Journal of Applied Meteorology and Climatology, 49(7), 1477–1495.

Kurino, T., 1997. A satellite infrared technique for estimating “deep/shallow” precipitation. Advances in Space Research, 19(3), 511–514.

Kwon, E., Sohn, B., Schmetz, J., & Wats, P., 2010. Intercomparison of height assignment methods for opaque clouds over the tropics. Journal of Atmospheric Sciences, 46(1), 11–19.

Lensky, I. M., & Rosenfeld, D., 2003a. A Night-Rain Delineation Algorithm for Infrared Satellite Data Based on Microphysical Considerations. Journal of Applied Meteorology, 42(9), 1218–1226.

Lutz, H-J., Inoue, T., & Schmetz, J., 2003. NOTESANDCORRESPONDENCE Comparison of a split-window and a multi-spectral cloud classification for MODIS observations. Journal of the Meteorological Society of Japan, 81(3), 623–631.

Mecikalski, J. R., & Bedka, K. M., 2006. Forecasting convective initiation by monitoring the evolution of moving cumulus in daytime GOES imagery. Monthly Weather Review, 134, 49–68.

Mecikalski, J. R., Bedka, K. M., Mackenzie, W. M., & Simon, J. P., 2007. Convective Initiation and Lightning Prediction: The potential of the MTG-FC imagery mission, Atmospheric Science Department, University of Alabama

in Huntsville, Cooperative Institute for Meteorological Satellite Studies University of Wisconsin- Madison Meteorological Satellite Conference, Amsterdam, The Netherlands, 24–28.

PAGASA, 2015. Climate of the Philippines. Retrieved December 15, 2015, from https://web.pagasa.dost.gov.ph/index.php/climate-of-the-philippines.

Santurette, P., & Georgiev, C. G., 2007. Water vapour imagery analysis in 7.3/6.2 μm for diagnosing thermo-dynamic context of intense convection. AMS-EUMETSAT.

Strabala, K. I., Ackerman, S. A., & Menzel, W. P., 1994. Cloud properties inferred from 8–12 micron data. Journal of Applied Meteorology, 33(2), 212–229.

Thies, B., Nauss, T., & Bendix, J., 2008a. Discriminating raining from non-raining cloud areas at mid-latitudes using Meteosat Second Genera- tion SEVIRI night-time data. Meteorological Applications, 15, 219–230.

Thies, B., Nauss, T., & Bendix, J., 2008b. Precipitation process and rainfall intensity differentiation using Meteosat Second Generation Spinning Enhanced Visible and Infrared Imager data. Journal of Geophysical Research, 113(D23), D23206.